Letter

Faraday-Rotation Atomic Magnetometer Using Triple-Chromatic Laser Beam

Yi Zhang,[1] Yuan Tian,[1] Songsong Li,[1,2] Jiehua Chen,[1] and Sihong Gu[1,*]

[1]*State Key Laboratory of Magnetic Resonance and Atomic and Molecular Physics, Wuhan Institute of Physics and Mathematics, Chinese Academy of Sciences, Wuhan 430071, China*
[2]*University of Chinese Academy of Sciences, Beijing 100049, China*

In this work, a single-laser-beam-based atomic Faraday-rotation magnetometer (FRM) scheme is studied in which atoms interact with a triple-chromatic laser beam. The circularly polarized carrier component of the beam prepares the atoms while its two orthogonal linearly polarized $\pm$1st sidebands are rotated oppositely and then measured. The study result reveals that the FRM scheme is suitable for implementation of a compact sensor supported by a fiber-coupled laser and is also suitable for implementation of a chip-scale sensor with a self-contained light source when using microelectromechanical systems (MEMS) technology.

I. INTRODUCTION

A number of different alkali vapor atomic magnetometers, including the nonlinear magneto-optical rotation magnetometer [1,2], the radio-optical double resonance magnetometer [3,4], the coherent population trapping (CPT) magnetometer [5,6], and the Faraday-rotation magnetometer (FRM) [7,8], have been studied. Among these magnetometers, mainly due to the better noise suppression effect [9], the FRM has been studied most extensively [10]. Working in the spin-exchange-relaxation-free (SERF) regime, FRM has achieved the sub-fT/$\sqrt{\text{Hz}}$ level of magnetic field detection sensitivity [11]; this order of sensitivity has only been realized previously when using superconducting quantum interference devices. Spatial resolution is another important aspect of magnetic field detection, and magnetometers with chip-scale sensors can be used to realize high-spatial-resolution detection applications such as measurements of biological fields [12–14] and detection of NMR signals [15,16].

In the conventional FRM configuration, the pump and probe beams are oriented orthogonally with respect to each other as they interact with the atoms. The resonant circularly polarized pump beam pumps the atoms into an anisotropic state and the off-resonant linearly polarized probe beam interacts with these anisotropic atoms, thus causing its polarization direction to be rotated because of the Faraday effect. The amount of rotation is detected and is used to provide the required information about the magnetic field.

The conventional FRM configuration is more difficult for chip-scale sensor implementation because of the difficulty involved in coupling the orthogonal beams into a single optical fiber. Shah and Romalis studied a single-monochromatic-beam-based FRM scheme that used elliptically polarized (EP) light to interact with the atoms. In their scheme (which was named the EPFRM scheme), the circularly polarized component of the EP light was used as the pump light, while the linear component was used as the probe light [17]. When using a fiber-coupled light source, compact and even chip-scale sensors can be realized using this scheme. However, the use of monochromatic light means that the pump and probe light beams cannot work at their optimal frequencies simultaneously, and a compromise frequency must thus be chosen to balance the pumping and probing efficiencies. Johnson *et al.* studied a bichromatic-beam-based FRM scheme in which a linearly polarized bichromatic beam from a polarization-maintaining fiber was converted into a circularly polarized and linearly polarized bichromatic beam for use as separate pump light and detection light beams, respectively, using an optical polarization converter. In principle, their scheme is also suitable for chip-scale sensor implementation. When supported by the use of two independent lasers, this scheme has the advantage that the pump/probe components can be adjusted independently to produce the best effect [18]; the technique was similarly employed in other works [19,20].

Here, we present our design for a single-beam FRM scheme and the results obtained from our experimental studies of this scheme. In the proposed scheme, a linearly polarized monochromatic laser beam is converted into a triple-chromatic laser beam through amplitude modulation

_____

*shgu@wipm.ac.cn

using an electro-optic amplitude modulator (EOAM). When the frequency difference between sidebands and carrier, f_m, is determined according to application needs and used as a modulation frequency, the frequencies of the ± 1st sidebands of the obtained triple-chromatic laser are $f_{\pm 1} = f_0 \pm f_m$, where f_0 is the carrier frequency.

II. POLARIZATION CONVERTER

The optical polarization converter (OPC) is designed as shown in Fig. 1, where an $(\hat{\mathbf{x}} + \hat{\mathbf{y}})/\sqrt{2}$ linearly polarized incident beam is split into $\hat{\mathbf{x}}$ and $\hat{\mathbf{y}}$ linearly polarized beams of equal intensity at the polarization reflecting surface of the polarizing beam splitter (PBS).

The initially $\hat{\mathbf{x}}$ linearly polarized beam, after traveling through the quarter waveplate (QWP1) $\rightarrow$ mirror (M1) $\rightarrow$ QWP1 path, is converted into a $\hat{\mathbf{y}}$ linearly polarized beam, while the initially $\hat{\mathbf{y}}$ linearly polarized beam, after traveling through the QWP2 $\rightarrow$ M2 $\rightarrow$ QWP2 path, is converted into a $\hat{\mathbf{z}}$ linearly polarized beam; the two coherent beams then combine into a single beam at the polarization reflecting surface of the PBS. However, when compared with the $\hat{\mathbf{y}}$ polarized combined beam, the $\hat{\mathbf{z}}$ polarized beam is phase delayed by

$$\Delta \Phi(f) = 4\pi \Delta L f / c, \qquad (1)$$

where ΔL is the optical path difference between the two combined beams, and f and c are the frequency and the speed of light, respectively. With regard to the linearly polarized triple-chromatic incident beam, when $\Delta \Phi(f_0) = \left(2n + \frac{1}{2}\right)\pi$, the ΔL of the two combined carriers is given by

$$\Delta L = (4n + 1)c/(8f_0) \qquad (2)$$

and the combined carrier becomes a right circularly polarized beam. If f_m is selected to satisfy

$$\Delta L = c/(8f_m), \qquad (3)$$

then by substituting Eq. (3) and $f_m = f_1 - f_0$ into Eq. (2), ΔL can be expressed as $\Delta L = (4n + 2)c/(8f_m)$; additionally, according to Eq. (1), $\Delta \Phi(f_1) = (2n + 1)\pi$. Therefore,
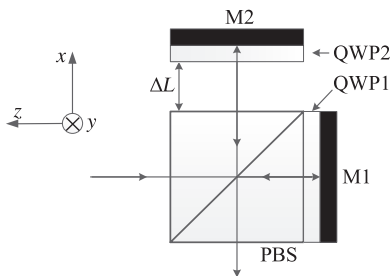

FIG. 1.   Optical polarization converter (OPC). PBS denotes the polarizing beam splitter; QWP, quarter waveplate; M, mirror.

the combined 1st sideband is linearly polarized. Similarly, $\Delta L = 4nc/(8f_{-1})$, and $\Delta \Phi(f_{-1}) = 2n\pi$ can be obtained, the combined -1st sideband is also linearly polarized. The phase difference of π between the combined ± 1st sidebands means that they are orthogonally polarized along $(\hat{\mathbf{y}} + \hat{\mathbf{z}})/\sqrt{2}$ and $(\hat{\mathbf{y}} - \hat{\mathbf{z}})/\sqrt{2}$, respectively.

Similarly, when $\Delta L = (4n - 1)c/(8f_0)$, with f_m satisfying $\Delta L = c/(8f_m)$, the triple-chromatic beam obtained is composed of the combined carrier that is left circularly polarized and the combined ± 1st sidebands where the 1st sideband is orthogonally linearly polarized along $(\hat{\mathbf{y}} - \hat{\mathbf{z}})/\sqrt{2}$ and the -1st sideband is similarly polarized along $(\hat{\mathbf{y}} + \hat{\mathbf{z}})/\sqrt{2}$.

According to Eqs. (2) and (3), the f_m can be expressed as $f_m = 8f_0/(4n + 1)$, and it is seen that there is no other restriction to f_m except that n is an arbitrary integer, so that it can be freely chosen in the range of interest according to application considerations.

When either of the light polarization combinations discussed above interacts with the alkali atoms in the magnetic field, the pump light's circularly polarized carrier prepares anisotropic atoms via resonant pumping, while the polarization directions of the two linearly polarized sidebands that act as the probe light are rotated because of their interactions with the anisotropic atoms. Because the rotated angle roughly satisfies the relation $\theta \propto (f - f_0)/[(f - f_0)^2 + \Gamma_f^2]$, where Γ_f is the linewidth [half width at half maximum (HWHM)] of the Doppler-broadened transition spectral line, the two sidebands rotate in opposing directions. This opposite rotation effect is used to realize FRM in the scheme studied in this work (which is defined as ORFRM).

III. EXPERIMENT

Under the existing conditions in our laboratory, we set up the tabletop single-beam FRM apparatus shown in Fig. 2. An external-cavity diode laser (ECDL) provides the 795-nm linearly polarized laser beam and an electro-optic phase modulator (EOPM) (NIR-MPX800-LN-10, iXblue) is used instead of the EOAM to modulate the light, so the laser beam is converted into a frequency-modulated multichromatic beam rather than the ideal triple-chromatic beam. For this application, the modulation is not strong and the higher-order sidebands share limited power, so the beam can be considered a pseudo-triple-chromatic beam. The sheet linear polarizer P1 is used to ensure perfectly linearly polarized light, and the half waveplate (HWP) is used to enable convenient rotation of the polarization direction during the experiments. After it is transmitted from the HWP, the linearly polarized pseudo-triple-chromatic beam is converted by the OPC into the required beam with the circularly polarized carrier and the orthogonal linearly polarized ± 1st sidebands. The beam splitter BS1 is arranged to split the beam for monitoring and analysis
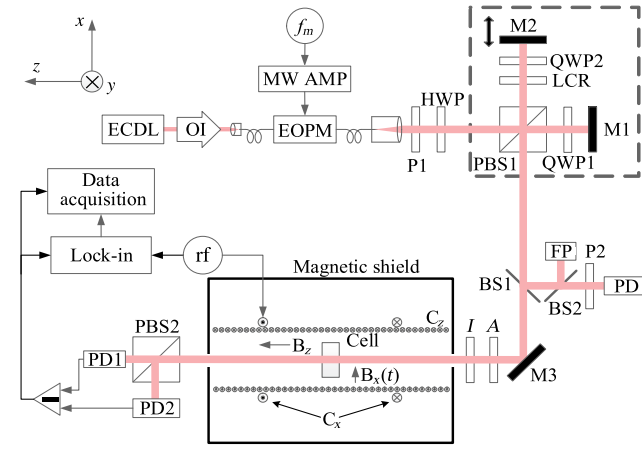
FIG. 2. Experimental setup. ECDL denotes the external-cavity diode laser; OI, optical isolator; EOPM, electro-optic phase modulator; f_m, microwave source; MWAMP, microwave amplifier; P, polarizer; HWP, half waveplate; PBS, polarizing beam splitter; QWP, quarter waveplate; M, mirror; LCR, liquid crystal retarder; BS, beam splitter; FP, Fabry-Perot interferometer; PD, photodetector; A, attenuator; I, iris; Cell, ^{87}Rb vapor cell; C_x, Helmholtz coils; C_z, solenoid; Magnetic shield, permalloy shell shield; rf, radiofrequency source; Lock-in, lock-in amplifier; Data acquisition, data recording system.

using the photodetector (PD) and the Fabry-Perot interferometer. The laser beam that is transmitted from the ^{87}Rb vapor cell is split by PBS2 and detected using PD1 and PD2, which are identical PDs.

In the experiments, f_0 is the $5S_{1/2}(F = 2)$ to $5P_{1/2}$ transition frequency, while f_m' and $\Delta L'$ are chosen preliminarily and determined using Eqs. (2) and (3) and $\Delta L' \approx c/(8f_m)$ is realized roughly using a precisely adjusted M2. We then scan the frequency of the monochromatic laser and obtain the curve shown in Fig. 3 from the output of the PD behind P2. At the frequency at which the curve reaches a maximum, the light is linearly polarized along the optical axis of P2, while at the minimum, it is perpendicularly linearly polarized relative to the optical axis. We select $f_m = \Delta f/2$, where Δf is the frequency difference between the frequencies at the maximum and the minimum of the curve, and then the preliminarily chosen $\Delta L'$ satisfies Eq. (3), i.e., $\Delta L' = \Delta L = c/(8f_m)$. We then leave the laser frequency at the zero detuning frequency of the curve from Fig. 3 and modulate the laser at f_m through the EOPM; the pseudo-triple-chromatic beam is thus obtained with a circularly polarized carrier and orthogonal linearly polarized $\pm$1st sidebands.

A liquid crystal retarder (LCR) (LCC1111-B, Thorlabs) is arranged so that $\Delta\phi$, the phase difference between the two combined light beams, can be adjusted precisely. During the experiment, we check the circularly polarized light beam by rotating P2 and monitoring the transmissive light. If the light intensity slightly deviates from the constant,
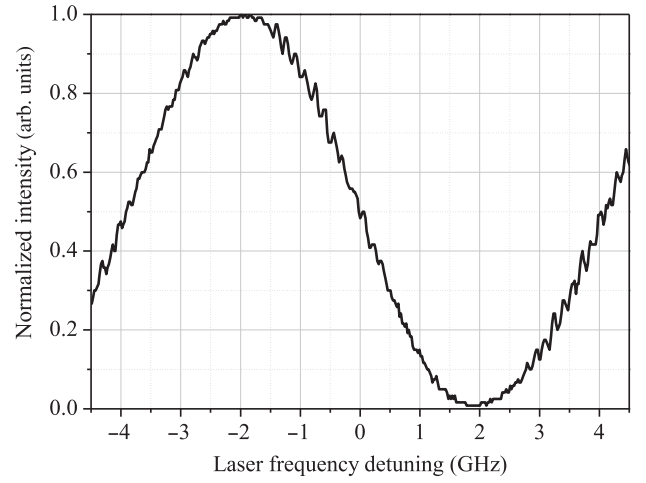

FIG. 3. PD output dependence on the laser frequency.

then LCR is used to finely adjust $\Delta\phi$ to reach a constant light intensity. As $f_0/f_m \sim 10^5$, we do not modify f_m when $\Delta\phi$ is adjusted because the experimental accuracy means that the change caused in ΔL is so small as to be negligible and the two sidebands can thus still be considered to be perfectly orthogonally linearly polarized.

In the experimental setup, the laser beam is reflected by M3, as shown in Fig. 2, which means that the two sidebands become $(\hat{x} \pm \hat{y})/\sqrt{2}$ [or $(\hat{x} \mp \hat{y})/\sqrt{2}$] linearly polarized. If there were no light-atom interactions, both sidebands would be split equally by PBS2; however, the light-atom interactions in the magnetic field cause the sidebands to rotate in opposite directions because of the Faraday-rotation effect. As a result, they both increase their contributions to one of the split beams and reduce their contributions to the other beam. In the experiments, the differential signal is obtained by subtracting the output from one PD from that of the other PD. The contributions to the differential signal should basically be from the $\pm$1st sidebands because the carrier and the even-order sidebands are circularly polarized, thus meaning that they are split equally, while the contributions from the odd higher-order sidebands are very limited.

The cylindrical glass cell used in the experiment is 10 mm long, has a diameter of 25 mm, and contains ^{87}Rb and a buffer gas composed of N_2 and CH_4 with a ratio of N_2:CH_4 = 1:2 at a pressure of 28.2 Torr. During the experiments, the cell temperature is stabilized at 85 °C. The solenoid C_z provides a static magnetic field, B_z, and the Helmholtz coils C_x provide the radiofrequency (rf) magnetic field $B_x(t)$. The outermost cylindrical permalloy shell shields the cell from any stray magnetic fields.

IV. RESULTS AND DISCUSSION

In the experiments, the ECDL provides a laser beam at the $5S_{1/2}(F = 2)$ to $5P_{1/2}$ transition frequency, and

because the bandwidth of the microwave amplifier (ZHL-1042J+, Mini-Circuits) used in the experiments is 0.01–4.2 GHz, we study the $f_m < 4$ GHz range. The experimental results show that when f_m is close to 3.4 GHz, the differential signal intensity obtained is reduced; this can be attributed to the $5S_{1/2}(F=1)$ to $5P_{1/2}$ reverse pumping effect from the second sideband.

The sensitivity (δB) corresponds to the smallest detectable change in the magnetic field is given by Ref. [21] $\delta B = 1/\gamma(\Delta\nu)/(S/N) = N/\gamma\Delta\nu/S$, where the magnetic resonance linewidth ($\Delta\nu$) is measured as HWHM, γ is the gyromagnetic ratio of the working atom, and S/N is the amplitude ratio between signal and noise. As the noise amplitude remains basically unchanged when f_m is varied in a small range, the optimized f_m is decided as $f_m \approx 2$ GHz according to the least $\Delta\nu/S$. Also, the noise amplitude remains basically unchanged when the EOPM input microwave power is varied, so the optical power distribution is also optimized by changing microwave power to reach the least $\Delta\nu/S$, with an 18-μW/mm^2-intensity pseudo-triple-chromatic incident beam. The optimized power distribution is that the carrier, the $\pm$1st sidebands, and the higher-order sidebands share 0.39, 0.54, and 0.07 of the total power respectively.

For comparison, we also study the EPFRM experimentally using the setup shown in Fig. 2. In the EPFRM study, the laser is not modulated and the monochromatic linearly polarized laser beam that is coupled out of the fiber is converted into an EP beam using the OPC. The ellipticity of the EP light is dependent on $\Delta\phi$, which is adjusted in the experiments using the LCR. Also, with an 18-μW/mm^2-intensity monochromatic incident laser beam and parameters optimized according to the least $\Delta\nu/S$, the obtained ellipticity is 0.4, and the optimized frequency is red-detuned by approximately 1.2 GHz from the central frequency, which is the frequency at which the maximal amplitude of the Doppler-broadened signal occurs.

Showing consistency with the independent elements, the OPC is sensitive to environmental vibrations, and we made considerable efforts during the experiments to suppress the vibrations and thus reduce the noise caused. This noise should be greatly reduced when the independent elements are integrated to form an integrated OPC device. We want to mention that in this experiment probe light detuning is chosen as 2 GHz on the consideration of a ^{87}Rb ground state hyperfine energy level split and the bandwidth of the used microwave amplifier. When the detuning is far larger than the hyperfine split of the working atom, a better effect can be expected. For example, if potassium were used as the working atom, with its several-hundred-MHz hyperfine split, the light detuning quantity would be selected more freely, a large detuning would be used for a better Faraday-rotation effect, the OPC device size would be smaller, and the vibration noise would be less coupled.
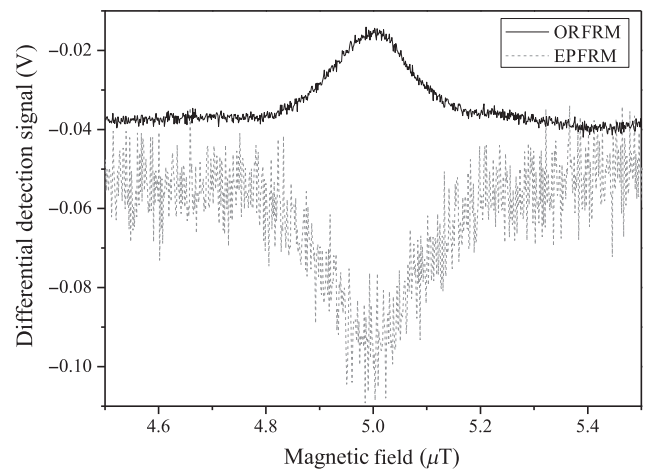

FIG. 4. The best differential detection signal curves of the ORFRM and EPFRM schemes obtained when the microwave power is input to EOPM is about 16 dBm and the incident laser intensity is 18 μW/mm^2. The ORFRM curve is recorded when the carrier, the $\pm$1st sidebands, and the higher-order sidebands share 0.39, 0.54, and 0.07 of the total power, respectively; the EPFRM curve is recorded when the ellipticity of the EP light is 0.4 and the frequency is 1.2 GHz red-detuned.

Figure 4 shows the magnetic resonance signal curves that are obtained experimentally from the two schemes by recording the differential signal while slowly ramping the static magnetic field B$_z$ around 5.0 μT. The dispersive signal curves are also obtained through shallow modulation of the frequency of the rf field B$_x$(t) at an audio frequency and recording the phase-sensitively demodulated output signal from the lock-in amplifier. The power spectral densities are then obtained by processing the data from the dispersive curves using a fast Fourier transformation, and Fig. 5 shows the power spectral densities that are recorded at magnetic resonance, that is, recorded at the maximal amplitudes of the two curves presented in Fig. 4.

It can be seen that the magnetic field sensitivity that is achieved using the ORFRM scheme is approximately 20 fT/$\sqrt{\text{Hz}}$, while with the EPFRM scheme, it is approximately 100 fT/$\sqrt{\text{Hz}}$; over the entire range of these curves, the sensitivity of the ORFRM is approximately five times better than that of the EPFRM.

The EPFRM is accompanied by a significant light shift effect because of the off-resonant light [17], while the light shift effect of the ORFRM, with its resonant pump light and symmetrically distributed probing light beams, should not only be much weaker than that of the EPFRM, but should also be weaker than that of the conventional FRM with its single off-resonant probing light beam [22].

The sensor of the EPFRM, for which the minimum volume is mainly restricted by the OPC, the glass cell, and PBS2, is not difficult to fabricate as an approximately 10-cm^3 compact sensor supported by a fiber-coupled laser.
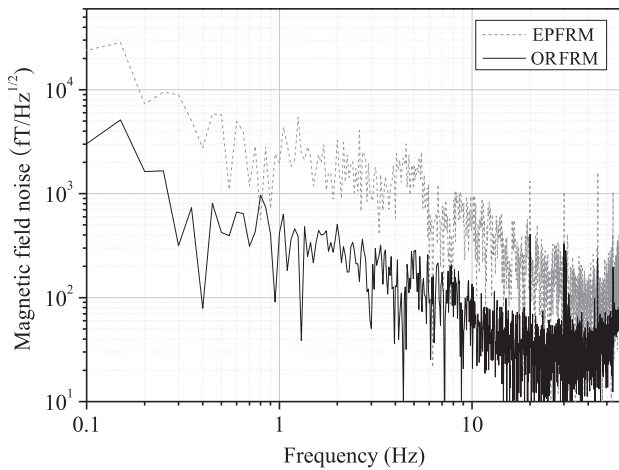
FIG. 5.   Magnetic field noise for the ORFRM and EPFRM schemes. The signal bandwidth is 200 Hz, which is set using the integration time of 5 ms. The signal recording time is 40 s, with a sampling rate of 2000 Hz. The other experimental parameters are the same as those used to produce Fig. 4.

Using microelectromechanical system (MEMS) technology, the sensor can be fabricated on the chip scale [23,24]. Because a vertical-cavity surface-emitting laser (VCSEL) can provide a frequency-modulated multichromatic linearly polarized divergent laser beam, it is also feasible to realize a chip-scale sensor with a self-contained light source.

When converting the divergent beam into the parallel one using the method that Fig. 2 of Ref. [25] described, a $20°$ divergent beam, a typical output beam of the VCSEL, can be converted into a 3-mm-diameter parallel one within 20 mm^3. Suppose that the two PBSs are both $3 \times 3 \times 3$ mm^3 cubes; then, through integration of a chip vapor cell, the detecting PBS, PDs, and other components, it is feasible to realize a chip-scale sensor with a volume of approximately 100 mm^3 and a self-contained light source. We should also note here that the laser frequency jitter-converted amplitude noise (FMAM noise), which will be significant in the chip-scale sensor, can be reduced considerably through a subtraction process using differential detection technology [26].

V. CONCLUSION

In conclusion, we propose and investigate a Faraday-rotation magnetometer scheme in which an amplitude-modulated triple-chromatic laser beam interacts with atoms. The circularly polarized carrier of the beam prepares the atoms. Then the orthogonal linearly polarized $\pm$1st sidebands are detected and their opposing Faraday rotations are extracted through a subtraction scheme (defined as the ORFRM scheme). The practicability of the scheme is studied experimentally using a frequency-modulated pseudo-triple-chromatic laser beam that is

obtained through frequency modulation of a monochromatic laser. Using the laboratory apparatus, detection sensitivity of 20 fT/$\sqrt{Hz}$ is achieved, which is five times better than the sensitivity of another single-beam scheme that was obtained under the same experimental conditions. The ORFRM sensor can be fabricated as a compact sensor when supported by a fiber-coupled laser beam, while use of MEMS technology could allow it to be fabricated as a chip-scale sensor with a self-contained light source.

[1] D. Budker, D. F. Kimball, S. M. Rochester, V. V. Yashchuk, and M. Zolotorev, Sensitive magnetometry based on nonlinear magneto-optical rotation, Phys. Rev. A **62**, 043403 (2000).

[2] V. V. Yashchuk, D. Budker, W. Gawlik, D. F. Kimball, Y. P. Malakyan, and S. M. Rochester, Selective Addressing of High-Rank Atomic Polarization Moments, Phys. Rev. Lett. **90**, 253001 (2003).

[3] W. E. Bell and A. L. Bloom, Optical detection of magnetic resonance in alkali metal vapor, Phys. Rev. **107**, 1559 (1957).

[4] P. D. D. Schwindt, B. Lindseth, S. Knappe, V. Shah, J. Kitching, and L. A. Liew, Chip-scale atomic magnetometer with improved sensitivity by use of the Mx technique, Appl. Phys. Lett. **90**, 081102 (2007).

[5] M. Fleischhauer and M. O. Scully, Quantum sensitivity limits of an optical magnetometer based on atomic phase coherence, Phys. Rev. A **49**, 1973 (1994).

[6] P. D. D. Schwindt, S. Knappe, V. Shah, L. Hollberg, J. Kitching, L. Liew, and J. Moreland, Chip-scale atomic magnetometer, Appl. Phys. Lett. **85**, 6409 (2004).

[7] J. C. Allred, R. N. Lyman, T. W. Kornack, and M. V. Romalis, High-Sensitivity Atomic Magnetometer Unaffected by Spin-Exchange Relaxation, Phys. Rev. Lett. **89**, 130801 (2002).

[8] D. Sheng, S. Li, N. Dural, and M. V. Romalis, Sub-femtotesla Scalar Atomic Magnetometry Using Multipass Cells, Phys. Rev. Lett. **110**, 160802 (2013).

[9] D. Budker and D. F. J. Kimball, *Optical Magnetometry* (Cambridge University Press, Cambridge, 2013).

[10] D. Budker and M. Romalis, Optical magnetometry, Nat. Phys. **3**, 227 (2007).

[11] I. K. Kominis, T. W. Kornack, J. C. Allred, and M. V. Romalis, A subfemtotesla multichannel atomic magnetometer, Nature **422**, 596 (2003).

[12] S. Knappe, T. H. Sander, O. Kosch, F. Wiekhorst, J. Kitching, and L. Trahms, Cross-validation of microfabricated atomic magnetometers with superconducting quantum interference devices for biomagnetic applications, Appl. Phys. Lett. **97**, 133703 (2010).

[13] T. H. Sander, J. Preusser, R. Mhaskar, J. Kitching, L. Trahms, and S. Knappe, Magnetoencephalography with a chip-scale atomic magnetometer, Opt. Express **64**, 1759 (2001).

[14] E. Boto, N. Holmes, J. Leggett, G. Roberts, V. Shah, S. S. Meyer, L. D. Muñoz, K. J. Mullinger, T. M. Tierney, S. Bestmann, G. R. Barnes, R. Bowtell, and M. J. Brookes, Moving magnetoencephalography towards real-world applications with a wearable system, Nature **555**, 657 (2018).

[15] M. P. Ledbetter, I. M. Savukov, D. Budker, V. Shah, S. Knappe, J. Kitching, D. J. Michalak, S. Xu, and A. Pines, Zero-field remote detection of NMR with a microfabricated atomic magnetometer, Proc. Natl. Acad. Sci. **105**, 2286 (2008).

[16] R. Jimenez-Martinez, D. J. Kennedy, M. Rosenbluh, E. A. Donley, S. Knappe, S. J. Seltzer, H. L. Ring, V. S. Bajaj, and J. Kitching, Optical hyperpolarization and NMR detection of ^{129}Xe on a microfluidic chip, Nat. Commun. **5**, 3908 (2014).

[17] V. Shah and M. V. Romalis, Spin-exchange relaxation-free magnetometry using elliptically polarized light, Phys. Rev. A **80**, 013416 (2009).

[18] C. Johnson, P. D. D. Schwindt, and M. Weisend, Magnetoencephalography with a two-color pump-probe, fiber-coupled atomic magnetometer, Appl. Phys. Lett. **97**, 243703 (2010).

[19] G. Bevilacqua, V. Biancalana, P. Chessa, and Y. Dancheva, Multichannel optical atomic magnetometer operating in unshielded environment, Appl. Phys. B **122**, 103 (2016).

[20] G. Bevilacqua, V. Biancalana, Y. Dancheva, and A. Vigilante, Self-Adaptive Loop for External-Disturbance Reduction in a Differential Measurement Setup, Phys. Rev. Appl. **11**, 014029 (2019).

[21] R. Jimenez-Martinez, W. C. Griffith, Y. J. Wang, S. Knappe, J. Kitching, K. Smith, and M. D. Prouty, Sensitivity comparison of Mx and frequency-modulated Bell–Bloom cs magnetometers in a microfabricated cell, IEEE Trans. Instrum. Meas. **59**, 372 (2010).

[22] M. Zhu, in *IEEE International Frequency Control Symposium* (IEEE, Geneva, Switzerland, 2007).

[23] R. R. Mhaskar, S. Knappe, and J. Kitching, in *IEEE International Frequency Control Symposium* (IEEE, Newport Beach, CA, USA, 2010).

[24] S. Woetzel, V. Schultze, R. Ijsselsteijn, T. Schulz, S. Anders, R. Stolz, and H. Meyer, Microfabricated atomic vapor cell arrays for magnetic field measurements, Rev. Sci. Instrum. **82**, 033111 (2011).

[25] J. F. Denatale, R. L. Borwick, C. Tsai, P. A. Stupar, Y. Lin, R. A. Newgard, R. W. Berquist, and M. Zhu, in *IEEE/ION Position, Location & Navigation Symposium* (IEEE, Monterey, CA, USA, 2008).

[26] V. Gerginov, S. Knappe, V. Shah, L. Hollberg, and J. Kitching, Laser noise cancellation in single-cell CPT clocks, IEEE Trans. Instrum. Meas. **57**, 789 (2008).